Deciphering core-exciton dynamics in CaF_2 with attosecond spectroscopy

Rafael Quintero-Bermudez and Stephen R. Leone
Department of Chemistry, University of California, Berkeley, California 94720, USA;
Chemical Sciences Division, Lawrence Berkeley National Laboratory, Berkeley, California 94720, USA;
and Department of Physics, University of California, Berkeley, California 94720, USA

(Received 6 October 2023; accepted 22 December 2023; published 17 January 2024)

Core excitons in solids have garnered increasing interest, yet their behavior and decay mechanisms are not fully understood. Here, we use attosecond extreme ultraviolet (XUV) transient absorption spectroscopy, performed with a broadband 25–45-eV sub-fs XUV pump pulse and a 500–1000-nm sub-5-fs near-infrared (NIR) supercontinuum probe pulse to monitor the excitation, dynamics, and decay of core excitons in CaF_2 at the Ca^{2+} $M_{2,3}$ edge. The XUV pulses are used to excite core excitons in CaF_2 based around the Ca^{2+} and the polarization of the medium is subsequently perturbed by the time-delayed NIR pulses to measure the spectral changes and decays. A number of features are identified in the transient absorption spectrum, which suggest transfer between excitonic states, Stark shifts, and the emergence of light-induced states. We find that various core excitons identified exhibit coherence lifetimes spanning 3–7 fs. Furthermore, a NIR-intensity-dependent analysis finds a negative correlation with the coherence lifetime of various identified excitonic features, supporting a phonon-mediated mechanism as responsible for the core-exciton decoherence. We present a computational band structure projection analysis strategy to estimate the orbital structure of the core excitons and determine which core-excitonic transitions should be allowed by selection rules with the probe beam. This strategy is found to successfully describe the observed spectroscopic data. The outlined joint spectroscopic and computational investigation of core excitons is a powerful technique that explains the complex behavior of core excitons in solid-state materials.

DOI: 10.1103/PhysRevB.109.024308

I. INTRODUCTION

Excitons, condensed matter quasiparticles that consist of a bound electron-hole pair [1], have been studied since the early seminal work of Frenkel [2], Wannier [3], and Peierls [4]. Exciton research has led to remarkable achievements in photovoltaics [5], light emission [6], solar water splitting [7], and a wide range of electronic devices [8]. Excitons that consist of a bound electron and a core hole, denominated core excitons, were identified in extreme-ultraviolet (XUV) and x-ray absorption spectra in the early 1970s due to increased accessibility of synchrotron radiation sources [9,10]. However, detailed understanding of the short-lived dynamics and decoherence of core excitons has only recently become possible with the development of few-femtosecond and attosecond XUV pump-probe spectroscopy techniques with tabletop high harmonic generation (HHG) sources [11–15]. HHG sources produce broad-spectrum XUV and soft x-ray pulses capable of supporting attosecond temporal resolution [16].

Core excitons are best observed in ionic insulators due to their relatively low dielectric constant and consequently weak screening effects. Core excitons have been observed in a wide range of large band-gap insulators [9]. Their absorption is often characterized by distinct strong and narrow absorption lines clearly visible at room temperature at a considerably large energy below the conduction band absorption, a quantity known as the binding energy. CaF_2 has been known to display a particularly distinct and strong absorption line in its XUV absorption spectrum [9,17,18], but the excitonic nature of this feature could not be confirmed. Furthermore, additional neighboring features were identified that also could not be conclusively identified as excitonic absorption.

Ultrafast pump probe spectroscopy studies have been conducted to investigate core excitons in only a handful of materials [11–14]. CaF_2 is an intriguing candidate to study core excitons given the doubly charged nature of the cation, its amenability to calculation, its rich XUV absorption spectrum, and the lack of data in the literature on its interpretation. Additionally, neither the Ca core levels nor fluorite crystal structure core excitons have been investigated, further motivating this study. The CaF_2 crystal structure is shown in Fig. 1(a), inset.

In many typical pump-probe XUV spectroscopy schemes, a near-infrared (NIR) or visible pump pulse is used to excite carriers in a sample, such as electrons across a band gap in semiconductors and insulators. This is followed by an XUV probe pulse to monitor time-resolved changes in the absorption spectrum. Core excitons, however, necessitate XUV or x-ray pump photons and the reversal of this pulse scheme. As a result, an attosecond XUV pulse is used first to pump core excitons and the NIR pulse is used second as the probe by perturbing the polarization of the medium, i.e., by modification of the core-exciton transition dipoles or exciting to neighboring core-exciton states. It worth noting that the experimental setup uses an XUV spectrometer, therefore the NIR *probe* pulse is not used as a traditional transient absorption probe used to determine changes in the NIR spectrum. Instead, the NIR probe is used to transiently alter the dynamics of states originally excited by the XUV pump (such as core excitons) to nearby

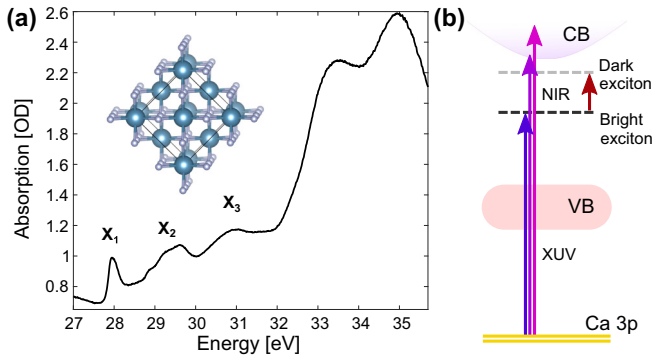

FIG. 1. Linear extreme ultraviolet (XUV) absorption spectrum of CaF_2 at the Ca $M_{2,3}$ edge. (a) Linear absorption spectrum of a CaF_2 thin film (25 nm) used in the transient absorption study. Inset: Crystal structure of CaF_2. (b) Schematic depiction of energy levels and bands involved in XUV pump–NIR probe experiments.

excited states or the continuum. This transient alteration of dynamics leads to features that can be observed in the XUV absorption spectrum. An excellent review on these types of experiments is reported in [19]. These measurements are not at risk of becoming overshadowed by valence band (VB) to conduction band (CB) carrier excitation due to the very large band gap in insulators such as CaF_2.

Here, we report on the core-exciton dynamics at the Ca^{2+} $M_{2,3}$ edge in the alkali-halide insulator CaF_2. This study consists of ultrafast XUV transient absorption spectroscopy (UXTAS) utilizing the XUV pump and NIR probe. The transient absorption measurements depict a rich array of time-dependent features in the 27-37-eV range. The features are used to identify resonant absorption of core-excitonic states, formation of light-induced states, Stark shifts, and charge transfer between core-excitonic states. Evidence is presented for the decay of the core-excitonic features to be interpreted as phonon mediated. A computational band structure projection strategy, consisting of density functional theory (DFT) and Bethe-Salpeter-equation (BSE) analysis, is presented to estimate the orbital structure of core excitons and to determine which core-excitonic transitions would be dipole allowed by selection rules with the NIR probe beam, most notably $\Delta l = \pm 1$ in photoexcited electronic transitions [20]. The outlined joint UXTAS and computational band structure projection analysis investigation of core excitons is a powerful technique that satisfactorily explains the complex behavior of core excitons in solid-state materials.

II. EXPERIMENTAL SCHEME

A detailed account of the experimental details is included in Appendix A. In brief, a sub-5-fs 500–1000-nm NIR probe pulse is incident on samples with a time delay after a 25–45-eV XUV pump pulse that is generated by HHG using the aforementioned NIR pulse incident onto a Kr gas cell. This NIR pulse modifies the decay of the polarization of the medium setup by the initiating XUV pulse. The time delay between the pulses is controlled by means of a retroreflector mounted onto a delay stage. The XUV beam is spectrally dispersed by a grating and recorded with an x-ray camera. Samples consist of 25-nm-thick CaF_2 thin films evaporated onto 30-nm-thick Si_3N_4 membrane substrates. The samples were characterized by powder x-ray diffraction to confirm the crystalline structure of the sample (Fig. S3 in the Supplemental Material [21]).

III. RESULTS

A. Transient absorption spectroscopy

The XUV absorption spectrum for a 25-nm-thick CaF_2 thin film is shown in Fig. 1(a). The distinct absorption peak at 28 eV (labeled X_1) has been attributed to a Γ-point core exciton forming between the photoexcited electron and the Ca^{2+} $3p$ core hole [9]. Hereafter, Ca^{2+} is simply indicated as Ca. The Ca $3p$ core levels are spin-orbit split but their energy separation is negligible such that the absorption spectrum cannot distinguish them [9]. Between 28.6 and 30 eV and 30 and 32 eV (labeled X_2 and X_3, respectively), a series of features are clearly observed. In previous work, these features were barely noticeable and were not interpreted. Here, we posit that these are also core excitons consisting of electrons from higher energy CB levels in CaF_2, and verify this assumption below via the transient spectra. The baseline absorption can be seen to increase after the X_1 feature. This is likely due to nonexcitonic excitation from the Ca $3p$ core levels to the CB. Finally, absorption is seen to increase significantly above 32 eV. This can be attributed to an increase in CB density as well as the excitation of F $2s$ core excitons to the CB.

A schematic of the UXTAS measurement is shown in Fig. 1(b). A broadband XUV pulse pumps Ca $3p$ core electrons into the CB and core excitons. The excited core excitons are subsequently probed with the NIR probe pulse. As mentioned earlier, the band gap of CaF_2 is far too large for electrons to be excited from the VB to the CB with the NIR pulse.

The UXTAS spectrum of the CaF_2 thin film collected with the highest NIR beam intensity or pulse energy used ($10.2\,TW/cm^2$ or 12 μJ, respectively) is shown in Fig. 2(a). As outlined above, positive time means that the XUV pulse arrives before the NIR pulse. Distinct transient features can be observed across the entire 27–37-eV range. Despite the high NIR intensity used, the observed transient absorption features are comparably weaker than those observed in previously studied core-excitonic systems, such as MgO [12]. Most features only seem to appear for the duration of the overlap of the XUV with the 5-fs NIR pulse. Three longer-lived features are observed that match the locations of X_1, and two regions within X_2. These are labeled A, B, and C in Fig. 2(a), respectively. In order to facilitate analysis, snapshots of the transient absorption at various time delays are presented as the change in absorption (or ΔOD) [Fig. 2(b)] and as total absorption [Fig. 2(c)]. The latter is presented with the ΔOD component multiplied by a factor of 10 and adding this to the static absorption to facilitate the observation of the weak changes in absorption.

Three types of features are identified: (1) increases in absorption at features Y_1, Y_2, Y_3, Y_4, and Y_5, (2) a bleaching of excitonic feature X_3, labeled Z, and (3) shifts in excitonic absorption features X_1 and X_2. The Y_n photoinduced absorption

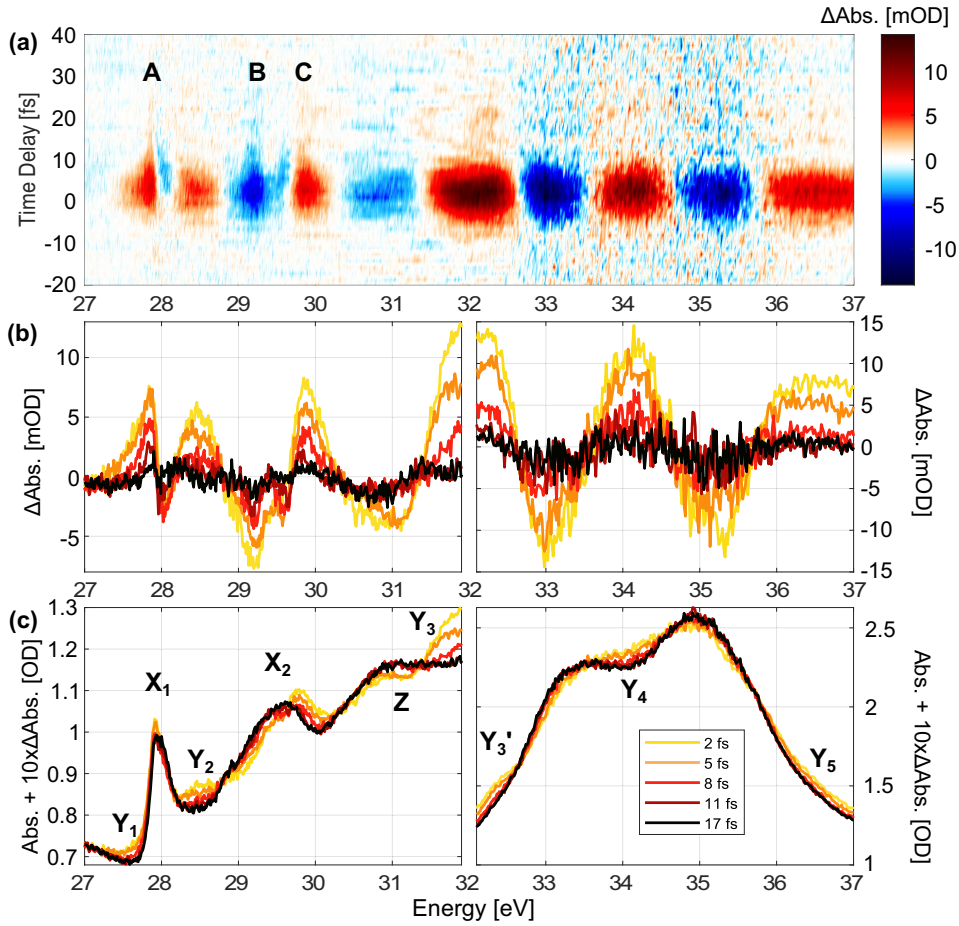

FIG. 2. Few-femtosecond dynamics of core excitons in CaF_2 observed by XUV transient absorption spectroscopy. (a) Delay-dependent transient absorption. Labels *A*, *B*, and *C* highlight longer-lived features, identifying them as core excitons. (b) Lineouts of delay-dependent transient absorption and (c) total absorption spectral traces taken at 2, 5, 8, 11, and 17 fs. The latter is plotted by adding the transient absorption component magnified by a factor of 10 to the static spectrum to facilitate observation of weak features. Labels X_n, Y_n, and *Z* identify excitonic features, photoinduced absorption, and bleaching, respectively.

features are ascribed to the emergence of light-induced states, as has been done for similar features in previous core-exciton dynamics studies on MgO [12]. $Y_{3–5}$, which consist of features well into the CB, however, could also result from renormalization of the band gap upon photoexcitation [22]. The bleach at *Z* might result from charge transfer from nearby core excitons, such as X_1 or those within the X_2 set of core excitons. There is an additional feature at 29.2 eV that could be attributed in part as a bleaching resulting from charge transfer. However, it is difficult to distinguish this potential effect from the shifts that are also observed. To determine the source of the excitonic shifts, the same experiment was conducted at various NIR intensities. In order to ascertain the shift in energy, features X_1 and X_2 are fitted by a sum of Gaussian functions in order to determine the shifts incurred by each component.

The results of the Gaussian fitting are presented in Figs. 3(a) and 3(b), for features X_1 and X_2, respectively. The energy shifts of each Gaussian component are plotted as a function of NIR peak intensity in Figs. 3(c) and 3(d), for features X_1 and X_2, respectively. The core-exciton shifts could result from the optical Stark effect [23] or could instead indicate transfer between core-excitonic states due to the NIR pulse [12]. The former is known to exhibit a linear increase with NIR intensity, whereas the latter is expected to exhibit a sublinear increase with NIR intensity, as noted in [12].

The measured peak shifts in feature X_1 are best described by a sum of a negative linear and a positive sublinear shift, which would correspond to a redshift due to the optical Stark effect and a blueshift due to excitonic transfer by the NIR field, respectively. From these observations, it can be inferred that the NIR energy (of 1.2–2.5 eV) is smaller than the energy difference between X_1 and a dark exciton *D* but that some transfer (albeit a small proportion of the excitonic population of X_1) is able to take place between these two features. The measured peak shifts in feature X_2 are all sufficiently well fitted by positive linear increases, i.e., blueshift due to an optical Stark effect. In this case it is inferred that the NIR energy is larger than the energy difference between X_2 and a dark exciton *D*' and that transfer between X_2 core excitons and *D*' must be negligible. This experiment, supported by the bleach of feature X_3 [labeled *Z* in Fig. 2(c)], suggests the existence of a dark exciton at approximately 31 eV.

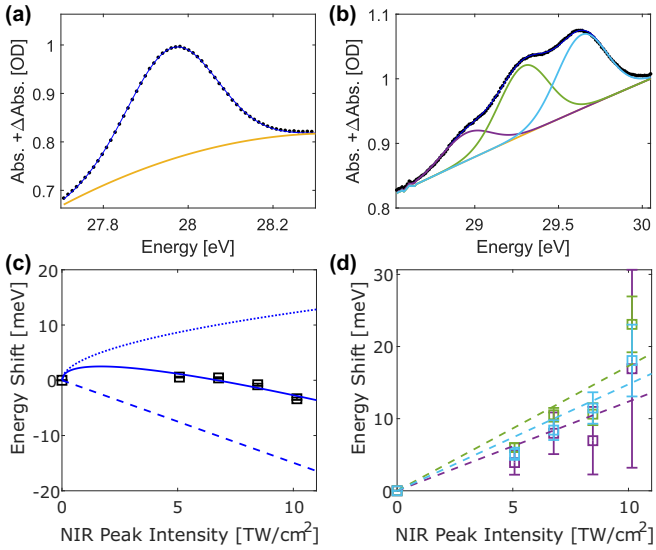

FIG. 3. Fitting of core-excitonic features at various NIR peak intensities reveal nature of spectral shifts. Fitting to one and three Gaussian functions, respectively, is used to fit total transient absorption spectra in excitonic features (a) X_1 and (b) X_2 after a subtraction of the baseline absorption. (c),(d) Energy shifts as a function of NIR peak intensities obtained from Gaussian fitting of excitonic features (a) X_1 and (b) X_2, respectively. Fitting consists of a positive sublinear term (excitonic transfer: dotted line) and negative linear term (Stark: segmented line) (total: full blue line) in X_1 and a sole linear term is found to describe energy shifts in X_2 adequately [Stark: segmented lines, colors in (b)].

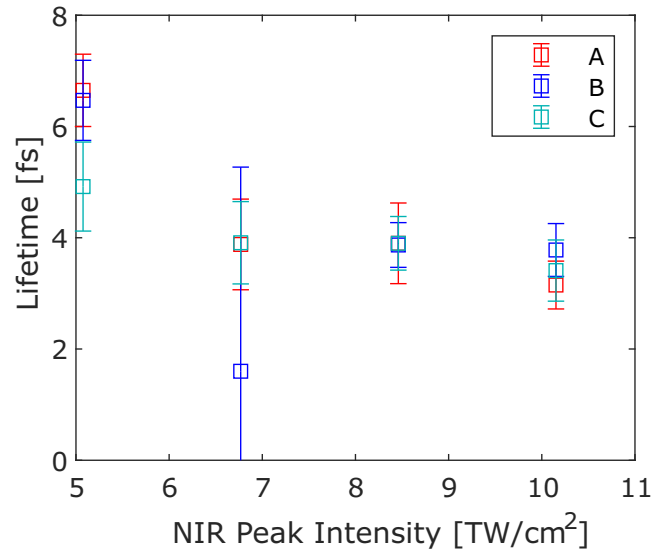

FIG. 4. Coherence lifetimes of core-excitonic features show a negative correlation with NIR peak intensity supporting a phonon-mediated decay. Lifetimes obtained from fitting the main transient component with a singular value decomposition of data around features *A*, *B*, and *C* to an exponentially modified Gaussian distribution function.

B. Core-exciton decay

The decoherence of core excitons in insulators has been debated in the literature since their discovery. Auger decay [24], electron-phonon coupling [12], electron-electron interactions [14], and mixing of core-exciton states [14] are a few of the most promising causes discussed in the literature. In order to provide evidence that might support a mechanism for core-exciton decoherence, the decay lifetimes of the three longer-lived features, albeit all three extremely short-lived, in the UXTAS [*A*, *B*, and *C* in Fig. 2(a)] were determined for various NIR intensities (Fig. 4). Singular value decomposition was used around features *A*, *B*, and *C* to ascertain the time-dependent trace. The decay of these features was then fitted with an exponentially modified Gaussian function (i.e., the convolution of Gaussian and exponential decay functions) in time to account for the instrument response function, which exhibits a Gaussian line shape due to the shape of the NIR pulse.

The measured coherence lifetimes of the core excitons decrease with increasing the NIR peak intensity. Although this property cannot single-handedly confirm a specific decoherence mechanism, it does support a phonon-mediated decay mechanism [11,12,25,26]. This is further discussed in the Discussion section, Sec. IV B below.

C. Computational modeling

DFT computations were used to understand the UXTAS results above. In particular, DFT was used to determine the conduction band levels that could be associated with each core-excitonic feature and the allowed transitions between them.

First, DFT computations were completed with the QUANTUM ESPRESSO software package [27,28] and were used to determine the projected band structure of CaF_2. This computation is illustrated in Fig. 5 depicting the projection of five core levels (Ca 3*p* and F 2*s*), all six VB levels, and six CB levels onto six electron orbitals: Ca 3*s*, Ca 3*p*, Ca 4*s*, Ca 3*d*, F 2*s*, and F 2*p*. It is observed that the core levels consist primarily of their expected electron orbitals, whereas the VB consists primarily of F 2*p* character. The CB is almost entirely Ca 3*d* type, with the exception of the CB edge near

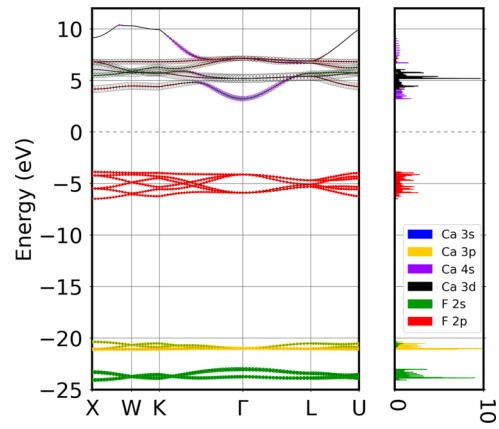

FIG. 5. Calculated band structure of CaF_2 suggests the orbital shapes of core, valence, and conduction band levels involved during UXTAS experiment. The projected band structure and projected density of states were calculated by using DFT.

the Γ point which corresponds to Ca 4*s* type and higher up CB levels (particularly in the vicinity of the Γ and *L* points) which exhibit some F 2*p* character.

Second, DFT computations with BSE were conducted with the EXCITING computational package [29,30] to determine the excitonic weight contributions of band structure levels to the linear absorption excitonic peaks. The result of these computations is illustrated in Fig. 6. Here, the computed linear absorption spectrum is shown in Fig. 6(a), which closely resembles the measured XUV absorption spectrum. On this figure, eight labels are placed throughout the spectrum highlighting representative spots within core-excitonic features. Next, wave functions are illustrated in real space for the first two highlighted spots within X_1 in the calculated absorption spectrum, Figs. 6(b) and 6(c). Interestingly, the shapes of these wave functions resemble *s* and *d* orbitals, respectively. It is found, however that excitonic weights plotted onto the band structure are more informative as to the orbital shape of the excitons, especially when coupled with the projected band structure in Fig. 5. With this in mind, band structures depicting excitonic weights are shown for all eight highlighted points in the XUV absorption spectrum in Figs. 6(d)–6(k).

The BSE computations find that the peak of X_1 can be associated with a strongly localized Γ-point exciton (in agreement with previous work [9]), which is of Ca 4*s* character, primarily [Fig. 6(d)]. Towards the higher-energy edge of the X_1 peak, other localized CB edge excitons with lower oscillator strengths can be found such as the *X*-point exciton in Fig. 6(e), which is of Ca 3*d* character, primarily. In the region that corresponds to the location of X_2 in the experimental data, one identifies excitons that seem more delocalized across the lowest CB level. As a result, it would be expected to exhibit a mix of Ca 4*s* and Ca 3*d* orbital shape with specific contributions depending on the region within the X_2 feature. It is ascertained that the remaining features correspond to the broad X_3 feature in the experimental data. This absorption peak seems to comprise core excitons consisting of delocalized contributions across higher levels in the CB. In particular, the higher energy region of this range of excitons exhibits contributions from the levels that begin to exhibit some F 2*p* character in addition to the Ca 4*s* and Ca 3*d* character that most of the core excitons appear to show.

IV. DISCUSSION

The experimental and computation results presented above present a cohesive explanation for the nature of the core-exciton absorption peaks in the linear spectrum, their transfers undergone during the XUV pump–NIR probe time-resolved experiment, and their decoherence mechanisms. A discussion on each of these topics is considered below.

A. Core-excitonic peaks and transfer

The experimental linear absorption spectrum consists of three main features before the rise in absorption at 32 eV due to Ca 3*p*-to-CB and F 2*s*-to-CB excitation: X_1, X_2, and X_3. All core excitons comprising these absorption features result from excitation from the Ca 3*p* core levels. X_1 is concluded to result from excitation to a band edge Γ-point core exciton and exhibits Ca 4*s* orbital shape. X_2, which appears to be made up of various excitonic features, is concluded to consist of core excitons delocalized across the CB edge and is expected to exhibit mixed Ca 4*s* and 3*d* orbital shape. The broad X_3 absorption is also expected to consist of various core excitons, in this case delocalized across higher CB levels, and is expected to exhibit mixed Ca 4*s* and 3*d* orbital shape. Interestingly the higher energy region of the X_3 feature also begins to exhibit F 2*p* orbital shape.

After the XUV pump, the 1.2–2.5-eV NIR probe enables core-excitonic transfer between the Γ-point core exciton in X_1 and the higher energy features in X_3 that exhibit F 2*p* orbital shape. This is a weakly allowed transition given the mixed Ca 4*s*, Ca 3*d*, and F 2*p* orbital shape of the X_3 excitons, and its transfer is further hampered by the weaker NIR intensity towards the edges of its broad spectrum. This transfer is evidenced by the bleaching *Z* feature, as well as the sublinear energy shift of X_1 vs NIR intensity. Transfer between the X_2 and X_3 excitons and between the X_1 and X_2 could not be identified. This might result from the transitions being disallowed due to more similar orbital angular momenta or due to too small an energy spacing between these sets of excitons compared to the NIR probe energy. It is also possible that transfer involving the X_2 feature takes place but is not possible to distinguish due to the several overlapping excitons within this feature.

We also note that it was unsuccessfully attempted to detect a transient ultrafast XUV signal due to the CaF_2 core excitons in a four-wave mixing experimental setup specialized for solid-state materials, similar to previous work [14]. This is attributed to weakly allowed transitions that will also lead to weak UXTAS signals, as discussed earlier. A detailed account of the four-wave mixing experimental setup and results will be detailed in a future report. Future work might also consider using a tunable and spectrally narrower XUV pulse (but still >1 eV bandwidth in order to resolve core-exciton lifetimes) in a similar experimental scheme in order to more clearly identify the particular core excitons involved in transfer events after a NIR probe beam.

B. Phonon-mediated core-exciton decoherence

Three relatively long-lived features are identified in the UXTAS data, labeled *A*, *B*, and *C*. The first is associated with the decoherence of the Γ-point exciton, whereas the latter two are associated with core excitons within X_2. All three excitonic features are directly excited by the initial XUV pump and then decohere over the course of a few fs. Their coherence lifetimes (spanning 3–7 fs for various excitons and intensities) are within the same range as those in MgO [12] and SiO_2 [11], where it was concluded that core excitons decohere as a result of electron-phonon coupling. These studies note that the phonon contribution to the dipolar phase decay can be described by (as detailed by Mahan [25]) $\mathrm{Im}(\varphi_{\mathrm{ph}}(t)) = \frac{M^2}{\omega_{\mathrm{ph}}^2}[(2N+1)(1-\cos\omega_{\mathrm{ph}}t)]$, which denotes Gaussian spectral line shapes when $\omega_{\mathrm{ph}}t \ll 1$. Other studies have cited Lorentzian line shapes as indicative of alternative decay pathways [14,15]. As illustrated in Fig. 3 , the spectral features of the CaF_2 core excitons are best fitted by Gaussian line shapes.

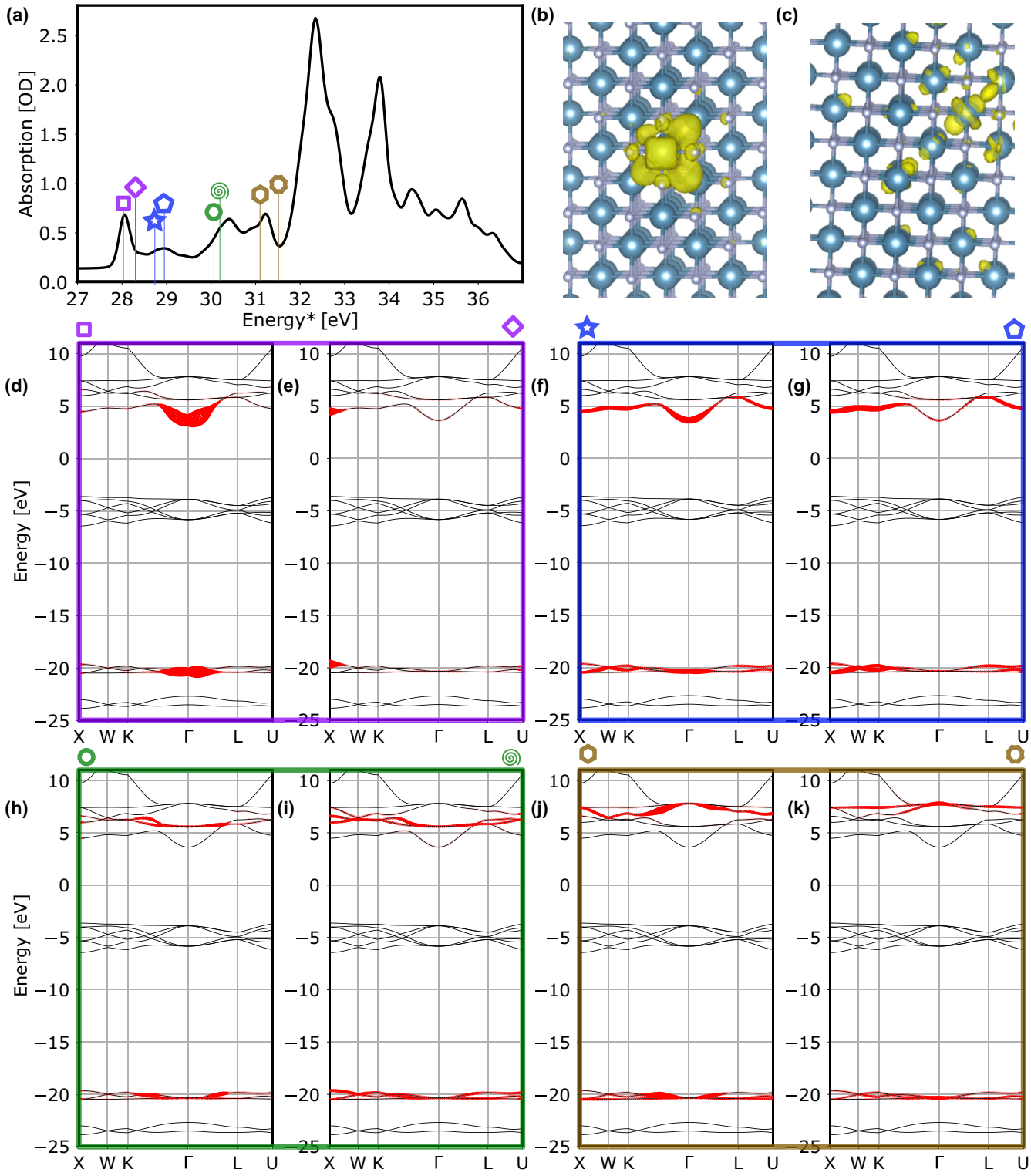

FIG. 6. Exciton computational analysis confirms the modes involved in the excitonic features and transfer. (a) Linear absorption spectrum with various representative excitons within each absorption peak. (b), (c) Excitonic wave functions for the purple square and diamond, respectively. (d)–(k) Excitonic weights depicted in red plotted on the CaF_2 band structure for the highlighted features on the spectrum in sequential order, i.e., purple square, purple diamond, blue star, blue pentagon, green circle, green spiral, yellow hexagon, and yellow eight-point star. Excitonic computational analysis performed with the EXCITING computational package using the Bethe-Salpeter equation (BSE).

Furthermore, much like in MgO and SiO_2, the expected Auger Lorentzian linewidth for a Ca $3p$ core level excitation would be 10 meV [31], which would result in a lifetime far longer than what we observe in CaF_2. As a result, the observed exciton decoherence cannot be attributed to Auger decay.

Additionally, the measurement of the coherence lifetime at various NIR intensities shows a decrease in the lifetime at increased probe intensity, further supporting a phonon-mediated decay mechanism. As the NIR peak intensity is increased, so is the phonon population by electron-phonon coupling. It is estimated from the core-exciton linear absorption linewidth (linewidth $\sigma = 102$ meV), after deconvolving the 10-meV Auger Lorentzian linewidth contribution, that approximately six phonons are generated per photon [32,33]. This was calculated by considering that the energy of the optical phonon involved would be between 31 and 55 meV [34]. Therefore, a large population of phonons will result from electron-phonon coupling upon excitation of the core exciton with the XUV, which could be responsible for the primary decay component observed in CaF_2's core excitons.

Thermal phonons are also a possibility as an alternative source of phonons that lead to the short coherence lifetimes observed here. The phonon population in CaF_2 will follow Bose-Einstein statistics and will increase as the temperature is increased [26]. Similarly, time-invariant features observed in UXTAS that are also present between pulses in 1-kHz repetition-rate experiments have been previously attributed to heat features in the literature [35]. It is therefore plausible that the time-independent thermal phonon population is also increased due to the high repetition rate NIR beam, such that an additional thermal phonon population might also contribute to the core-exciton decoherence. It is proposed that both electron-phonon coupling upon XUV excitation and a thermal phonon population that increases due to the high intensity NIR beam could contribute to core-exciton decoherence. Further experiments need to be designed in order to distinguish each individual contribution.

V. CONCLUSION

In summary, core excitons in CaF_2 at the $M_{2,3}$ edge were observed and studied by UXTAS. Various core excitons excited directly from the Ca $3p$ core levels were identified within the XUV linear absorption region between 27 and 37 eV. Excitonic transfer was ascertained between a bright Γ-point core exciton that exhibits Ca $4s$ orbital shape and a weakly visible core exciton that exhibits mixed F $2p$, Ca $4s$, and Ca $3d$ orbital shapes. The decay of the excitonic features is concluded to result from phonon-mediated decoherence, namely electron-phonon coupling. This study sought to understand the behavior of core excitons in CaF_2, as well as to illuminate the general behavior of core excitons in solid-state materials. Additionally, the joint approach involving experimental UXTAS and computational modeling consisting of projections onto the band structure is presented as a successful method to understand the rich behavior and interactions of core excitons in solids.

ACKNOWLEDGMENTS

This work was supported by Air Force Office of Scientific Research (AFOSR) Grant No. FA9550-20-1-0334. R.Q.B. acknowledges support from a Natural Sciences and Engineering Research Council of Canada (NSERC) postdoctoral fellowship under Grant No. 557315.

APPENDIX A: EXPERIMENTAL METHODS

An apparatus was constructed to specifically measure attosecond XUV pump probe spectroscopy in solid-state materials and will be further detailed in a future report. The experiments use spectrally broad and temporally short pulses to evaluate a large spectral region at attosecond scales. The NIR and XUV pulses in the-UXTAS experiment are produced by a Ti : sapphire laser (Coherent Astrella, 1 khz repetition rate, 7 mJ pulse energy, 35 fs pulse duration, and 32 nm bandwidth). 3 mJ of the beam is focused with an $f = 2.5 -$ m dielectric concave mirror into a 2.2-m long hollow core fiber (inner diameter 700 μm) filled with an Ar gas pressure gradient (approximately 5 Torr to 120 mTorr) to generate a supercontinuum spanning 500–1000 nm wavelength with self-phase modulation (Fig. S2 in the Supplemental Material [21]). Eight pairs of double angled broadband chirped mirrors (Ultrafast Innovations, PC1332), fused silica wedge pairs, and potassium dihydrogen phosphate (KDP) wedge pairs are optimized to compensate accumulated dispersion and temporally compress the pulses to ∼5 fs duration. The beam is then split by a 90:10 broadband beam splitter. The former is subsequently focused into a gas cell with a 200-μm hole with Kr gas at ∼15 Torr in a vacuum chamber held at $\sim 10^{-7}$ Torr to generate broadband XUV pulses via HHG. A 100-nm Al foil filter (Lebow Company) is then used to filter out the NIR and transmit the XUV pulse, which is focused onto the sample with a gold-coated toroidal mirror. The remaining NIR beam after the beam splitter is used as the probe beam. The NIR probe is delayed with respect to the XUV beam with a piezo stage (Physik Instrumente, P-620.1CD). The NIR probe is then focused into the vacuum chamber system with a $f = 1$ meter concave mirror. The beam is incident onto the sample off-axis from the XUV beam by a small angle ($\theta = 23$ mrad) in order to focus both beams onto the sample accurately without clipping. The pulse energy of the NIR beam is adjusted with an iris and monitored with a power meter between 6 and 12 μJ. The NIR beam diameter is characterized using a beam profiler (DataRay WinCamD). Temporal and spatial overlap is determined by placing an Ar gas cell in the interaction region instead of the sample. Time zero is estimated by fitting the rise time of the Ar $3s3p6np$ autoionization signal to an exponentially modified Gaussian function. The NIR pulse width is estimated to be under 5 fs with a dispersive characterization of ultrafast pulses (D scan, Sphere Ultrafast Photonics) (Fig. S1 in [21]) and confirmed with the rise time of the Ar $3s3p6np$ autoionization signal. The spectral energies are also calibrated with the autoionization lines of Ar $3s3p6np$ [36]. Another 100-nm Al foil is then used to filter out any remaining NIR; meanwhile the XUV beam is spectrally dispersed by a gold-coated flat-field grating (01-0639, Hitachi) and measured with an XUV charge-coupled device camera (Pixis XO 400-B, Princeton Instruments).

The samples measured are 25 nm polycrystalline CaF_2 thin films (Lebow Company) evaporated onto 30-nm-thick Si_3N_4 membranes (Norcada NX5050X). The samples are mounted

on a $xy-$axis translation stage (Physik Instrumente). The illuminated area is refreshed every 5 min using vertical and horizontal sample translation to avoid artifacts from sample heating and damage.

APPENDIX B: COMPUTATIONAL METHODS

The projected band structure of CaF_2 is calculated using the plane-wave DFT software package QUANTUM ESPRESSO. We use Perdew-Burke-Ernzerhof (PBE) projector augmented wave (KJPAW) functionals, some of the most commonly used generalized gradient approximation (GGA) functionals due to their versatility, and a k grid of $8 \times 8 \times 8$. GGA functionals build on local-density approximation (LDA) functionals that only depend on electron density at each coordinate, by using functionals that are also dependent on the gradient of the electron density. Optimal k grid dimensions were determined by a series of convergence computational tests.

The excited state band structure projections are computed using the computational package exciting, which is a full-potential all-electron package implementing linearized augmented plane-wave methods. Excited state properties are calculated with the Bethe-Salpeter equation and visualized with EXCITING. First, a ground state calculation is completed using PBE GGA functionals and a k grid of $8 \times 8 \times 8$. The BSE formalism [30] is then used with EXCITING to compute bound two-particle states. In the context of optical absorption, the BSE formalism is used to describe electron-hole pair excitations, including excitons. In the optical absorption calculation, a Gaussian broadening is applied by convolving the discrete absorption lines produced by the computation with a Gaussian function (with $\sigma = 100$ meV to match that of the experimental core-exciton absorption spectra); this empirically reflects the inhomogeneous broadening in the system, which as discussed earlier is mostly due to phonon broadening. This value was estimated by using experimental broadening linewidths for linear absorption spectra as a reference and is within values typically used for calculating absorption spectra in solids [29].

For the Bethe-Salpeter-equation calculations, six core levels (Ca $3s$, Ca $3p$, and F $2s$), all six VB levels, and six CB levels are used to calculate all excited states within the 27–37-eV absorption region (after scissor correction). A scissor correction is used to match the DFT-computed absorption spectrum with the experimental spectrum to make up for DFT's underestimation of the band gap. Excitonic weights are then visualized in k space by projecting the two-particle electron-hole wave functions resulting from the BSE computation into a basis of electron and hole levels, or more specifically into a sum of ground state valence and conduction levels.

[1] R. S. Knox, Theory of excitons, *Solid State Physics*, Vol. 1 (Academic Press Inc., New York, 1963), pp. 1–58.

[2] J. Frenkel, On the transformation of light into heat in solids. I, Phys. Rev. **37**, 17 (1931).

[3] G. H. Wannier, The structure of electronic excitation levels in insulating crystals, Phys. Rev. **52**, 191 (1937).

[4] R. Peierls, Zur theorie der absorptionsspektren fester körper, Ann. Phys. **405**, 905 (1932).

[5] G. D. Scholes and G. Rumbles, Excitons in nanoscale systems, Nat. Mater. **5**, 683 (2006).

[6] M. Yuan, L. N. Quan, R. Comin, G. Walters, R. Sabatini, O. Voznyy, S. Hoogland, Y. Zhao, E. M. Beauregard, P. Kanjanaboos, Z. Lu, D. H. Kim, and E. H. Sargent, Perovskite energy funnels for efficient light-emitting diodes, Nat. Nanotechnol. **11**, 872 (2016).

[7] F. Fassioli, R. Dinshaw, P. C. Arpin, and G. D. Scholes, Photosynthetic light harvesting: excitons and coherence, J. R. Soc. Interface **11**, 20130901 (2014).

[8] L. V. Butov, Excitonic Devices, Superlattices Microstruct. **108**, 2 (2017).

[9] G. W. Rubloff, Far-Ultraviolet reflectance spectra and the electronic structure of ionic crystals, Phys. Rev. B **5**, 662 (1972).

[10] W. Gudat, C. Kunz, and H. Petersen, Core exciton and band structure in LiF, Phys. Rev. Lett. **32**, 1370 (1974).

[11] A. Moulet, J. B. Bertrand, T. Klostermann, A. Guggenmos, N. Karpowicz, and E. Goulielmakis, Soft x-ray excitonics, Science **357**, 1134 (2017).

[12] R. Géneaux *et al.*, Attosecond time-domain measurement of core-level-exciton decay in magnesium oxide, Phys. Rev. Lett. **124**, 207401 (2020).

[13] M. Lucchini *et al.*, Unravelling the intertwined atomic and bulk nature of localised excitons by attosecond spectroscopy, Nat. Commun. **12**, 1021 (2021).

[14] J. D. Gaynor, A. P. Fidler, Y.-C. Lin, H.-T. Chang, M. Zuerch, D. M. Neumark, and S. R. Leone, Solid state core-exciton dynamics in NaCl observed by tabletop attosecond four-wave mixing spectroscopy, Phys. Rev. B **103**, 245140 (2021).

[15] H. T. Chang, A. Guggenmos, C. T. Chen, J. Oh, R. Géneaux, Y. De Chuang, A. M. Schwartzberg, S. Aloni, D. M. Neumark, and S. R. Leone, Coupled valence carrier and core-exciton dynamics in WS_2 probed by few-femtosecond extreme ultraviolet transient absorption spectroscopy, Phys. Rev. B **104**, 064309 (2021).

[16] P. M. Kraus, M. Zürch, S. K. Cushing, D. M. Neumark, and S. R. Leone, The ultrafast x-ray spectroscopic revolution in chemical dynamics, Nat. Rev. Chem. **2**, 82 (2018).

[17] T. Mabuchi, H. Toda, and H. Yamanaka, Core exciton of alkali and alkali-earth halides, J. Phys. Soc. Jpn. **62**, 246 (1993).

[18] J. Frandon, B. Lahaye, and F. Pradal, Spectra of electronic excitations in CaF_2, SrF_2, and BaF_2 in the 8 to 150 EV range, Phys. Status Solidi **53**, 565 (1972).

[19] M. Wu, S. Chen, S. Camp, K. J. Schafer, and M. B. Gaarde, Theory of strong-field attosecond transient absorption, J. Phys. B: At. Mol. Opt. Phys. **49**, 62003 (2016).

[20] P. Hamm and M. Zanni, *Concepts and Methods of 2D Infrared Spectroscopy* (Cambridge University Press, Cambridge, UK, 2011).

[21] See Supplemental Material at http://link.aps.org/supplemental/10.1103/PhysRevB.109.024308 for NIR pulse temporal and spectral characterization data, X-ray diffraction data of sam-

ple, linear absorption spectral fitting comparisons between Lorentzian and Gaussian lineshapes, and transient absorption data acquired with various NIR pulse powers, which includes Refs. [37–42].

[22] C. V. Shank, R. L. Fork, R. F. Leheny, and J. Shah, Dynamics of photoexcited GaAs band-edge absorption with subpicosecond resolution, Phys. Rev. Lett. **42**, 112 (1979).

[23] M. Combescot, Semiconductors in strong laser fields: from polariton to exciton optical stark effect, Phys. Rep. **221**, 167 (1992).

[24] G. J. Lapeyre, A. D. Baer, J. Hermanson, J. Anderson, J. A. Knapp, and P. L. Gobby, Photoemission studies of core exciton decay in KI, Solid State Commun. **15**, 1601 (1974).

[25] G. D. Mahan, Emission spectra and phonon relaxation, Phys. Rev. B **15**, 4587 (1977).

[26] N. W. Ashcroft and N. D. Mermin, *Solid State Physics* (Cengage Learning, New York, 1976).

[27] P. Giannozzi *et al.*, Advanced capabilities for materials modelling with QUANTUM ESPRESSO, J. Phys.: Condens. Matter **29**, 465901 (2017).

[28] P. Giannozzi *et al.*, QUANTUM ESPRESSO: a modular and open-source software project for quantum simulations of materials, J. Phys.: Condens. Matter **21**, 395502 (2009).

[29] A. Gulans, S. Kontur, C. Meisenbichler, D. Nabok, P. Pavone, S. Rigamonti, S. Sagmeister, U. Werner, and C. Draxl, Exciting: a full-potential all-electron package implementing density-functional theory and many-body perturbation theory, J. Phys.: Condens. Matter **26**, 363202 (2014).

[30] E. E. Salpeter and H. A. Bethe, A relativistic equation for bound-state problems, Phys. Rev. **84**, 1232 (1951).

[31] K. Ueda, J. B. West, N. M. Kabachnik, Y. Sato, K. J. Ross, H. J. Beyer, H. Hamdy, and H. Kleinpoppen, Evolution from spectator to normal auger lines through the thresholds observed in the Ca 3*p* excitation region, Phys. Rev. A **54**, 490 (1996).

[32] R. D. Carson and S. E. Schnatterly, Phonon coupling to core spectra in homopolar semiconductors, Phys. Rev. B **39**, 1659 (1989).

[33] P. H. Citrin, P. Eisenberger, and D. R. Hamann, Phonon broadening of x-ray photoemission linewidths, Phys. Rev. Lett. **33**, 965 (1974).

[34] G. Petretto, S. Dwaraknath, H. P. C. Miranda, D. Winston, M. Giantomassi, M. J. Van Setten, X. Gonze, K. A. Persson, G. Hautier, and G. M. Rignanese, High-Throughput density-functional perturbation theory phonons for inorganic materials, Sci. Data **5**, 180065 (2018).

[35] H. Liu, I. M. Klein, J. M. Michelsen, and S. K. Cushing, Element-specific electronic and structural dynamics using transient XUV and soft x-ray spectroscopy, Chem. **7**, 2569 (2021).

[36] R. P. Madden, D. L. Ederer, and K. Codling, Resonances in the photo-ionization continuum of Ar I (20-150 eV), Phys. Rev. **177**, 136 (1969).

[37] B. Alonso, Í. J. Sola, and H. Crespo, Self-Calibrating d-scan: measuring ultrashort laser pulses on-target using an arbitrary pulse compressor, Sci. Rep. **8**, 3264 (2018).

[38] P. Zaumseil, High-Resolution characterization of the forbidden Si 200 and Si 222 reflections, J. Appl. Crystallogr. **48**, 528 (2015).

[39] R. W. G. Wyckoff and R. W. G. Wyckoff, *Crystal Structures* (Interscience, New York, 1963), Vol. 1.

[40] T. Hom, W. Kiszenik, and B. Post, Accurate lattice constants from multiple reflection measurements. ii. lattice constants of germanium silicon, and diamond, J. Appl. Crystallogr. **8**, 457 (1975).

[41] K. Momma and F. Izumi, VESTA 3 for three-dimensional visualization of crystal, volumetric and morphology data, J. Appl. Crystallogr. **44**, 1272 (2011).

[42] A. L. Patterson, The Scherrer formula for x-ray particle size determination, Phys. Rev. **56**, 978 (1939).